Enhanced Photoacoustic Detection of Heparin in Whole Blood *via* Melanin Nanocapsules Carrying Molecular Agents

Wonjun Yim,

Materials Science and Engineering Program, University of California San Diego, La Jolla, California 92093, United States

Kathryn Takemura,

ENSCO, Inc., Melbourne, Florida 32940, United States

Jiajing Zhou,

Department of Nanoengineering, University of California San Diego, La Jolla, California 92093, United States

Jingcheng Zhou,

Department of Nanoengineering, University of California San Diego, La Jolla, California 92093, United States

Zhicheng Jin,

Department of Nanoengineering, University of California San Diego, La Jolla, California 92093, United States

Raina M. Borum,

Department of Nanoengineering, University of California San Diego, La Jolla, California 92093, United States

Ming Xu,

Department of Nanoengineering, University of California San Diego, La Jolla, California 92093, United States

Corresponding Author: Jesse V. Jokerst – *Materials Science and Engineering Program, Department of Nanoengineering, and Department of Radiology, University of California San Diego, La Jolla, California 92093, United States*; jjokerst@eng.ucsd.edu.

Supporting Information

The Supporting Information is available free of charge at https://pubs.acs.org/doi/10.1021/acsnano.1c08178.

Materials and methods, TEM image of PBDT-TA core nanoparticles, UV–vis–NIR spectra of PBDT-TA and PBDT-TA@PDA, TEM image with different PDA thicknesses, schematic describing Michael addition and Schiff base reaction, colloidal stability of PNC, fluorescence of dye-loaded PNC, images and size distribution of PBDT-TA, PBDT-TA@PDA, and PNC collected by NTA, loading capacity of PNC, PA signal of PNC only, surface charge-dependent PA signal, PA spectra of PNC@NB, concentration-dependent PA signal, photograph of PNC@NB-heparin interaction, PA signal stability of PNC@NB, PA response of PNC@ NB with/without protamine, linear correlation between ACT and cumulative heparin, colloidal stability of PNC@NB, hemolysis of PNC@NB, photograph of proposed functional optic fiber, computational images of PNC@NB-heparin aggregation (PDF)

PDA–heparin interactions with NB dye (MOV)

PDA–heparin interactions without NB dye (MOV)

Complete contact information is available at: https://pubs.acs.org/10.1021/acsnano.1c08178

Yong Cheng,
Department of Nanoengineering, University of California San Diego, La Jolla, California 92093, United States

Tengyu He,
Materials Science and Engineering Program, University of California San Diego, La Jolla, California 92093, United States

William Penny,
Division of Cardiology, VA San Diego Healthcare System, University of California San Diego, La Jolla, California 92093, United States

Bill R. Miller III,
Department of Chemistry, Truman State University, Kirkville, Missouri 63501, United States

Jesse V. Jokerst
Materials Science and Engineering Program, Department of Nanoengineering, and Department of Radiology, University of California San Diego, La Jolla, California 92093, United States

Abstract

Photoacoustic (PA) imaging has proved versatile for many biomedical applications from drug delivery tracking to disease diagnostics and postoperative surveillance. It recently emerged as a tool for accurate and real-time heparin monitoring to avoid bleeding complications associated with anticoagulant therapy. However, molecular-dye-based application is limited by high concentration requirements, photostability, and a strong background hemoglobin signal. We developed polydopamine nanocapsules (PNCs) *via* supramolecular templates and loaded them with molecular dyes for enhanced PA-mediated heparin detection. Depending on surface charge, the dye-loaded PNCs undergo disassembly or aggregation upon heparin recognition: both experiments and simulation have revealed that the increased PA signal mainly results from dye-loaded PNC–heparin aggregation. Importantly, Nile blue (NB)-loaded PNCs generated a 10-fold higher PA signal than free NB dye, and such PNC enabled the direct detection of heparin in a clinically relevant therapeutic window (0–4 U/mL) in whole human blood ($R^2 = 0.91$). Furthermore, the PA signal of PNC@NB obtained from 17 patients linearly correlated with ACT values ($R^2 = 0.73$) and cumulative heparin ($R^2 = 0.83$). This PNC-based strategy for functional nanocapsules offers a versatile engineering platform for robust biomedical contrast agents and nanocarriers.

Graphical Abstract
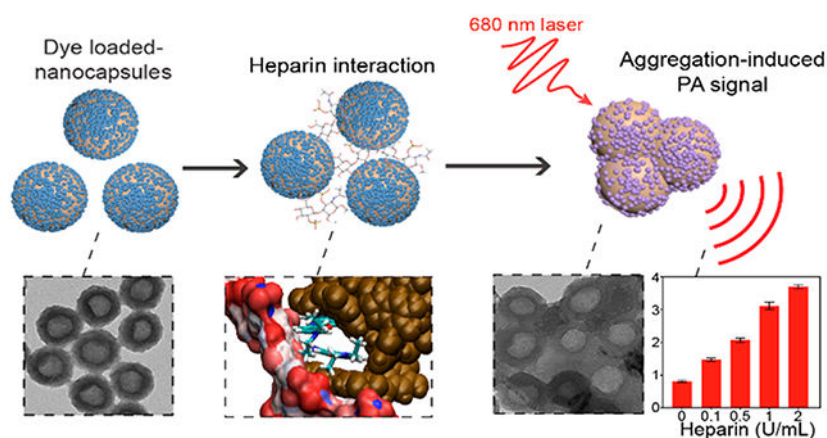
INTRODUCTION

Heparin-based anticoagulant drugs—including unfractionated heparin, low molecular weight heparin, and synthetic heparin—are key elements of surgical and cardiovascular medicine to prevent blood clots, but bleeding risks associated with anticoagulants require close monitoring to prevent heparin overdose.[1–5] Infants are particularly susceptible to heparin overdoses due to their small weight and the possibility of miscalculation of dosage level.[6–8] Thousands of children have suffered from hemorrhages or emboli, and infant deaths have been attributed to heparin errors.[7,9] The conventional toolkit for monitoring heparin activity uses activated coagulation-time assays, *e.g.*, activated partial thromboplastin time (aPTT), anti-Xa analysis, and activated clotting time (ACT).[10] aPTT has been widely used to monitor heparin; however, it suffers from long turnaround times and can be impacted by variations (*e.g.*, sample volume, diurnal changes, fibrinogen).[11] While the anti-Xa test is not impacted by collection tubes or fibrinogen, it is costly and requires extensive sample processing (~1 h).[12] Lastly, all these tools are limited by the low frequency of sampling, which means they are limited to periodic determination.[13,14] Thus, a variety of methods have been proposed to provide real-time information on heparin anticoagulation therapy.

Photoacoustic (PA) imaging has advantages versus other alternatives for monitoring heparin (Table S1). For example, fluorescence-based methods are sensitive but can be difficult to use in biological conditions, *e.g.*, serum and whole blood.[15–19] Fluorescence is also difficult to use in biological tissues due to light scattering, while the PA signal can propagate through the tissue and monitor specific biological events.[20] Colorimetric methods are simple but are limited to color changes in whole human blood.[21–23] Heparin detection in whole human blood is valuable because it can avoid drawing blood and does not require blood fractionation to collect plasma. It can expedite the sensing process, thus closely monitoring heparin in real time. Electrochemical methods allow for heparin sensing in whole blood, but they still require elaborate pretreatments: blood samples were diluted 100-fold with

PBS and 5 mM of potassium ferrocyanide.[24–26] All these methods also have yet to be broadly studied for clinical care (Table S1). In contrast, PA imaging is real-time and noninvasive and can directly monitor heparin without any pretreatments even in whole human blood. Therefore, PA imaging is proposed here to improve the standard of care in monitoring heparin.[27–30] PA imaging uses a light in–sound out approach, where the light excites target materials to generate acoustic waves detected by ultrasonic transducers.[31] A previous study demonstrated that PA imaging can monitor heparin in whole human blood *via* methylene blue (MB) dye. An increased PA signal of MB dye was a function of heparin concentration due to strong MB–heparin association that improves heat transfer.[27] However, the use of free molecular dyes to monitor heparin suffers from several drawbacks such as high concentration requirements (*e.g.*, 1 mM of free MB dye), photostability, and broadly interfering background signal from hemoglobin.[27,32–34] Incorporating these molecular dyes into a rigid nanostructure is an effective method to overcome the above limitations by modulating the PA-related processes (*e.g.*, optical absorbance, fluorescence quenching, photoprotection, heat confinement, and heat transfer).[35–39] For example, indocyanine green (ICG)-loaded mesoporous silicon nanoparticle (MSN) showed higher PA performance than free ICG dye due to low thermal conductivity of MSN.[37] However, synthesizing porous nanostructures often requires strong acidic solvents (*e.g.*, hydrofluoric acid) for template removal and tedious shell fabrication (*e.g.*, layer-by-layer).[37,40,41]

In this work, we report polydopamine nanocapsules (PNCs) loaded with small molecular dyes to monitor heparin *via* PA imaging (Scheme 1a). Instead of other templates (*e.g.*, polymer, silica, and metal nanoparticles), we used a simple supramolecular template which is size-tunable (*e.g.*, 50–650 nm) and highly stable in various aqueous conditions (*e.g.*, acidic and alkaline environments) but can readily disassemble in organic solvents (*e.g.*, dimethylformamide (DMF)).[41,42] Using supramolecular networks, we successfully developed a synthetic hollow melanin that has superior loading capacity over a compact polydopamine (PDA) nanoparticle. Furthermore, various molecular dyes can be easily loaded into the nanocapsule due to the desirably adhesive nature of PDA originated from catechol groups.[43,44] We empirically demonstrated multiple noncovalent interactions (*e.g.*, electrostatic, π–π stacking, hydrophobic interactions) that are involved in dye–PNC assemblies and validated them with molecular dynamic (MD) simulations. These dye-loaded PNCs showed exceptional PA enhancement compared to the free molecular dyes due to the lower thermal conductivity of PDA, fluorescence quenching, local concentration of free dyes, and photoprotection. Specifically, dye-loaded PNC generated 10-fold PA enhancement over free dye at the same dye concentration. Our results also revealed two phenomena: (1) surface charge-dependent disassembly (*i.e.*, release) of dyes from PNC and (2) aggregation of dye-loaded PNC during heparin interaction (Scheme 1b). Intriguingly, heparin-mediated aggregation of dye-loaded PNC led to a decreased optical absorbance with a concurrent increase in PA signal. The increased PA signal is likely due to the reduced degrees of freedom of particles that induced poor heat transfer and increased the thermal gradient between aggregates and solvent.[45] This PDA-enabled strategy highlights the approach of designing functionalized nanocapsules for enhanced PA imaging with increased insight into the PA mechanism occurred in nanoparticles.

RESULTS AND DISCUSSION

Synthesis of Dye-Loaded PNC.

Six mg of natural polyphenol (*e.g.*, tannic acid, TA) and 3 mg of aromatic dithiol (*e.g.*, benzene-1,4-dithiol, BDT) precursors are used to make polymerized BDT nanoparticles (referred as PBDT-TA) that serve as simple sacrificial templates.[42] First, we synthesized monodispersed PBDT-TA nanoparticles, where the size was easily tunable from 70 to 120 nm by increasing the concentration of BDT from 0.5 to 1.25 mg mL^{-1} at a fixed concentration of TA at 0.5 mg mL^{-1} (Figure S1). PDA was then coated on the PBDT-TA forming a highly uniform core–shell nanoparticle (PBDT-TA@PDA) as clearly observed by transmission electron microscopy (TEM) (Figure 1a, Figure S2, and Figure S3). The removal of the PBDT-TA templates with DMF led to monodisperse PNCs that were 30 nm thick (Figure 1b and Figure S4). The rugged surface morphology of the PNC is shown in scanning electron microscopy (SEM) images (Figure 1c). Energy-dispersive X-ray spectroscopy (EDX) revealed that PNC was composed of C, N, and O. The low signal of S in EDX indicated that PBDT-TA templates were successfully removed. The voids were observed in the high-angle annular dark-field-scanning transmission electron microscopy (HAADF-STEM) images (Figure 1d).

We then loaded diverse dyes into the nanocapsules. The preliminary results showed that adding positively charged dyes directly into the negatively charged PNC causes particle aggregation due to strong electrostatic attraction (data not shown). To prevent particle aggregation and improve colloidal stability, we used HS-mPEG (M_w 5k Da) to interact with catechol functional groups in PDA *via* a Michael reaction (Figure S5). Notably, the PEGylated PNCs showed great loading capacity with higher colloidal stability than sodium dodecyl sulfated (SDS)-modified PNCs (Figure S6). Four representative molecular dyes (*e.g.*, MB, Nile Blue (NB), Azure A (AA), and Neutral Red (NR)) were chosen for heparin sensing and successfully loaded in PEGylated PNC (referred as PNC@XX, XX = MB, AA, NB, and NR). Against PNC that features a broadband absorbance, dye-loaded PNC showed distinct absorption spectra relative to the cargo's absorption: PNC@MB, PNC@AA, PNC@NR, and PNC@NB showed maximum absorption wavelengths at 666, 614, 482, and 620 nm, respectively (Figure 1e). Likewise, dye-loaded PNC emitted dye-specific fluorescence behaviors while PNC alone showed no inherent fluorescence (Figure S7).

The color of the solution changed from brown (PNC) to dark green (PNC@MB), red (PNC@NR), or blue (PNC@NB and PNC@AA) after dye encapsulation (Figure 1f). The negatively charged surface of PNC (−27.7 ± 0.1 mV) increased to −21.8 ± 0.2 mV (PNC@AA), − 16.7 ± 1.0 mV (PNC@NR), −16.0 ± 0.6 mV (PNC@MB), and −5.3 ± 0.6 mV (PNC@NB) because of the loaded positively charged dyes (Figure 1g). Dynamic light scattering (DLS) data showed that PNC, PNC@MB, PNC@AA, PNC@NR, and PNC@NB had narrow size distributions (polydispersity index (PDI) < 0.1). The hydrodynamic diameter of the PNC increased (~55 nm) due to the loaded dyes (Figure 1h). Monodispersed PBDT-TA@PDA and PNC were observed using nanoparticle tracking analysis (NTA) that further verified the size distribution of nanoparticles from DLS data (Figure 1i and Figure S8).

Multiple Interactions in the Dye–PNC Assemblies.

PDA is composed of abundant amine and catechol groups, and thus, it can accommodate multiple noncovalent interactions (*e.g.*, hydrogen bonding, electrostatic, π–π stacking, hydrophobic interactions) that enable it to efficiently load a variety of small molecular dyes.[46,47] More free dye was loaded in the PNC where the surface of PNC was less PEGylated as confirmed by DLS and absorbance (Figure 2a and Figure S9). This is because PEG neutralizes the surface charge and the steric bulk of PEG reduces dye-PDA interactions (Figure S10).[48] However, the PEGylated PNC enabled a 3-fold increase in dye loading efficacy in a basic solvent (pH 8.5) over water due to PDA deprotonation (Figure S11). Furthermore, the PEGylated PNCs showed higher loading efficiency of MB (81%), AA (80%), and NB (73%) dyes compared to PDA nanoparticles: MB (72%), AA (71%), and NB (60%) (Figure 2b). Correspondingly, the dye-loaded PNC featured a 1.3-fold higher absorption peak than the dye-loaded solid PDA nanoparticles, indicating that hollow PDA nanostructure can load more dyes due to the 1.73-fold increased surface area (Figure S12).[40]

MB, AA, and NB dyes are positively charged, and heterocyclic aromatic molecules that contain *p*-orbital electrons. These dyes can potentially interact with PDA through a variety or combination of noncovalent interactions such as hydrophobic, π–π, and electrostatic interactions.[49] To corroborate which interactions govern the stability of different dye–PDA assemblies, PNC@MB, PNC@AA, and PNC@NB were all incubated in 10 mM of NaCl, HCl, NaOH, urea, Triton X-100, DMSO, DMF, and SDS (Figure 2c,d). First, DMSO and DMF are organic solvents that can break π–π interactions:[50] PNC released the loaded MB, AA, and NB dyes under the organic solvents as a result of π–π interactions being interrupted. Second, SDS or TritonX-100 are surfactants that can destroy ionic or nonionic interactions.[51] Likewise, PNC released the loaded dyes under the ionic or nonionic surfactants due to the disassembly of weak ionic or hydrophobic interactions. Lastly, PNCs also released the loaded dyes in acidic condition (pH ≈ 2), but there was no release of the loaded dye in 10 mM of NaOH (pH ≈ 12), NaCl, and urea that can destroy hydrogen bonding. Thus, we conclude that electrostatic, hydrophobic, and π–π interactions were involved in the formation of PNC@MB, PNC@AA, and PNC@NB.

Molecular dynamics (MD) simulations were also conducted to further validate the forces contributing to the interaction of PDA, dyes (*e.g.*, MB and NB), and heparin (Figure 2e). Decomposition analysis through the Molecular Mechanics Poisson–Boltzmann Surface Area (MMPBSA) approach yielded the magnitude and sign of the forces associated with the interaction of the dye, heparin, and PDA. Electrostatic and Van der Waals (VDW) energetic contributions dramatically stabilized the interaction of heparin, dyes, and PDA (Figure 2e). The electrostatic portion is associated with the interaction of the positively charged dye and the negatively charged sulfate groups on heparin. The VDW fraction is clearly mostly associated with the PDA. Nonpolar solvation is correlated with the change in surface area and entropic contributions when aggregates of PDA form. While the energetic contribution of nonpolar solvation is comparatively very small, it is a slightly stabilizing force, as is shown in the small negative value. Finally, polar solvation, which describes the process of solvating a moiety, was found as destabilizing force with respect to the interaction of PDA, heparin, and the dyes. Collectively, it is clear that the energetics of the dye–which is

dominated by electrostatic interactions with heparin but also has contributions from VDW interactions with PDA–is necessary to facilitate the interaction between PDA and heparin.

Release of the Loaded Dye in Negatively Charged PNC.

We previously showed that free dyes can interact with heparin for increased PA signal.[27] To identify the dyes' roles in this study, PNC@MB, PNC@AA, and PNC@NB were centrifuged four times to completely remove free dyes in the solution (Figure S13). Then, PNCs loaded with 50 μM of MB, AA, or NB dye were incubated with heparin from 0 to 5 U/mL, which led to optical and PA changes. During this interaction, the color of the solution rapidly changed within 1 min (Figure 3a). Consequently, the absorbance peak of each nanocapsule (MB, AA, and NB) decreased and blue-shifted; the fluorescence largely attenuated (Figure 3b and Figure S14).

We suspect that the loaded dye could be competitively extracted from the PNC due to strong local electrostatic attractions between the dye and heparin.[45] To verify this, PNC@MBs were spun down to collect the supernatant after they were incubated with heparin. The absorbance obtained from the supernatant was consistent with the absorbance of free MB dye–heparin interactions, indicating release of the loaded MB dyes (Figure 3c and Figure S15). Moreover, there was a slight decrease in hydrodynamic diameter of PNC@MB, PNC@AA, and PNC@NB upon incubation with heparin while maintaining its hollow structure without shrinking or disassembly of the PDA shell during the interactions (Figure 3d,e). It is noteworthy that PNC alone did not undergo any change in absorbance, fluorescence, hydrodynamic diameter, or PA intensity after interaction with heparin (Figure S16). However, the release of the loaded dyes from the PNC led to a decrease in PA intensity (Figure 3f). We hypothesized that incorporating the free dyes into PNC greatly enhances PA performance of the free dyes due to four reasons: (1) PDA's 4-fold lower thermal conductivity of PDA ($k_{PDA} \approx 0.13$) than water ($K_{water} \approx 0.59$), (2) fluorescence quenching of free dyes, (3) local concentration of loaded dyes as opposed to free state, and (4) the ability to protect the dyes from thermal degradation; the disassembly of dye–PNC assemblies would therefore expose free dyes, resulting in decreased PA signal.[37,38]

To verify this mechanism, we compared PA signal of dye-loaded PNCs and free dyes with different concentrations from 10 to 1000 μM. Notably, background-corrected PNC@MB, PNC@AA, and PNC@NB showed 10-fold higher PA signal compared to the free MB, AA, and NB dyes at the same concentration (50 μM) (Figure 3g). We also confirmed that dye-loaded PNCs showed 90% fluorescence quenching of free dyes and generated higher PA signal than free dye–heparin interactions (Figure 3h and Figure S17). These results indicate that the release of the loaded dye from PNC decreases PA signal due to decreased local concentration of the loaded dyes in PNC and relatively lower PA signal generated from the released dye–heparin interactions.

PA Enhancement of Positively Charged PNC.

The surface charge of dye-loaded PNCs is dependent on the amount of the loaded dye, while the colloidal stability relies on the net surface charge after conjugation with heparin. Encouraged by our results, another routine for sensing heparin was developed (Figure

4a). After loading a higher amount of NB dye (~80 μM) into PNC, PNC@NB showed a positively charged surface (+8.5 mV). However, PNC@MB and PNC@ AA still showed a negatively charged surface at the same loading concentration (Figure S18). Intriguingly, there was an increase in PA intensity when positively charged PNC@NB interacted with heparin either in water ($R^2 \approx 0.82$) or whole human blood ($R^2 \approx 0.91$), while negatively charged PNC@NB (−7.0 mV) inversely showed a decrease in PA signal (Figure 4b, Figure S18, and Figure S19). The limit of detection of PNC@NB was 0.063 U/mL in water and 0.14 U/mL in whole human blood. A sample of 8×10^6 particles/mL is required to induce PNC@NB–heparin aggregation (Figure S20). Furthermore, positively charged PNC@NBs loaded with 80 μM dye showed higher PA signal over free NB dye of 5 mM when they interacted with heparin in whole human blood (Figure S21).

PNC@NB showed particle aggregation as a function of heparin concentration that increased the PA signal, as confirmed by size, surface charge, photograph, and decreased absorbance in water (Figure 4c, Figure S22, and Figure S23). This finding is significant because the mechanism of PA signal generation has been understood by the conventional thermoelastic expansion model where the optical absorption of the nanoparticle is proportional to PA signal generation.[20] We believe that the PNC@NB–heparin aggregation may enhance thermal conductivity and could improve heat transfer or the fluorescence that quenched during the aggregation can contribute to heat generation (Figure S23).[38] This aggregation-induced PA enhancement showed a stable PA signal for 15 min, and the induced PA signal was reversible when protamine (known heparin antagonist)[52] was added to the interaction (Figure S24 and Figure S25).

Importantly, we tested PNC@NB with clinical specimens collected from 17 patients undergoing a cardiac procedure that required a high dose of heparin infusion. This work shows that our approach is not measuring just heparin concentration but also clotting time:[53] The PA signal of PNC@NB was linearly increased as a function of cumulative heparin (R^2 = 0.83) and ACT values (R^2 = 0.73) (Figure 4d). In addition, ACT values were linearly correlated with cumulative heparin (R^2 = 0.91) (Figure S26). Collectively, this prototype of heparin sensing system can linearly generate the PA signal in whole human blood as well as clinical specimens, demonstrating great promise for medical applications. Furthermore, PNC@NB showed high colloidal stability in different media (*e.g.*, DMEM, plasma, 2.5 or 5% of human serum) (Figure S27).

To further investigate the specificity of the aggregation-induced PA signal, PNC@NBs were incubated with other complex sample matrices such as bovine serum albumin (BSA), hemoglobin (Hgb), human-pooled plasma, thrombin, Dulbecco's modified Eagle Medium (DMEM), poly(sodium-4-strynesulfornate) (PSS), relevant ions (*e.g.*, Cl$^-$, Ca^{2+}), heparin analogue (*e.g.*, chondroitin sulfate (Chs)),[15] and heparin at the same mass concentration (2 μg/mL), respectively. Although it is generally accepted that electrostatic-mediated particle interaction has poor specificity, there was a significant increase in PA signal when PNC@NB interacted with heparin due to induced PNC@NB–heparin aggregation (Figure 4e). Our previous study showed that free NB dye can interact with heparin, causing aggregation that increased the PA signal.[32] Likewise, the increased PA signal of PNC@NB was due to the induced PNC@NB-heparin aggregation, which corresponds to the

increased size of PNC@NB (PDI > 0.5 in heparin) (Figure 4f). Notably, PNC@NB in other biomolecular conditions (*e.g.*, BSA, plasma, and thrombin) showed small polydispersity (PDI ~ 0.2) and hydrodynamic diameter compared to PNC@NB in heparin (Figure 4f). The induced PNC@NB aggregation during heparin sensing was also clearly observed by TEM images (Figure 4g). The PA signal of PNC@NB is proportional to particle concentration, and PNC@NB showed no hemolysis (Figure S20 and Figure S28). The PA response from PNC@NB had a linear correlation with aPTT values at a heparin concentration of 0.2–1 U/mL (Figure S29). Taking advantage of the adhesive nature of PDA, small molecule dyes could be coated on inert materials (Figure S30), suggesting the potential use of this dye-PNC scaffold for functionalizing catheters to monitor heparin.

Lastly, MD simulations were used to further investigate the interactions of heparin with the PNC@NB. The aggregation of PDA began quickly (~2 ns) along with the formation of the PDA@NB (Figure 4h and Movie S1). Negatively charged heparin interacted strongly with the positively charged NB dyes, which resulted in the formation of the PNC@NB-heparin complex (Figure S31) to subsequently crosslink the PNC and induce aggregation. However, there was no observed aggregation between heparin and PDA alone (Figure S32 and Movie S2). To quantitatively evaluate PNC@NB–heparin interactions, all possible distances were measured between all possible combinations of all PDA molecules with each heparin monosaccharide in the simulation. This distance data was then analyzed to elucidate the number of "individual interactions", *i.e.*, interactions between PDA and a monosaccharide unit that was not present within the past 10 frames of the simulation to avoid double counting the same interaction. Over 130 ns of unrestrained simulation, the simulation with NB dye present had 645 individual interactions between heparin and PDA. This stands in stark comparison to the simulation with no dye present and had only 90 individual interactions between heparin and PDA (Figure 4i). This explains the experimentally observed dye-loaded PNC–heparin aggregation; there was no interaction between PNC alone and heparin (Figure 4c and Figure S16).

CONCLUSIONS

We developed small molecular dye–PNC nanosystems as a viable heparin-sensitive platform for PA imaging due to the adhesive nature, fluorescence quenching, and low thermal conductivity of PDA. These dye–PDA assemblies allow quantitative heparin monitoring *via* enhanced PA signal generation. We validate mechanisms that were present in the significant PA enhancement of dye-loaded PNC compared to the free dyes. Comprehensive insights of charge-dependent aggregation of dyes–PNC versus disassembly of dyes–PNC were highlighted to better understand the on/off PA amplification. Encouraged by this results, future work includes the development of advanced heparin sensing platform (*e.g.*, functionalizing catheter) for *in Vivo* PA imaging and the use of other molecular agents to increase sensitivity for the heparin detection.[54–56] This PDA-enabled strategy for designing functionalized nanocapsules will provide better pathway for tailoring diverse molecular contrast agents and expand approach of eliciting PA signal for biomedical applications.

METHODS

Experimental Section.

Synthesis of PBDT-TA Nanoparticles.—For synthesis of PBDT-TA nanoparticles with a diameter of 80 nm, 375 μL of TA solution (16 mg mL^{-1} in water) was added to 12 mL of bicine buffer (pH 8.5, 10 mM) under vigorous stirring at 1200 rpm.[42] Then, 1.44 mL of BDT solution (4 mg mL^{-1} in DMF) was added and stirred for 12 h. The size of PBDT-TA nanoparticles was tunable by adding more BDT solution at the fixed TA concentration. The resulting PBDT-TA nanoparticles were purified by centrifugation (9000g for 10 min) twice to remove the excess complexes. The pellet was resuspended in water for future use.

Synthesis of PBDT-TA@PDA Core–Shell Nanoparticles.—The concentrated PBDT-TA nanoparticles were first dispersed in 8 mL of bicine buffer (10 mM, pH 8.5) followed by the addition of 1 mL of dopamine solution (4 mg mL^{-1} in water) under vigorous stirring at 1200 rpm for 12 h. The color of the solution changed from white to dark brown as polydopamine was coated on the PBDT-TA nanoparticles. The resulting product was purified by centrifugation (9000g for 10 min) twice. The thickness of the PDA coating is tunable from 25 to 100 nm by adjusting the amount of dopamine solution from 1.0 to 6.0 mg mL^{-1} while fixing the concentration of PBDT-TA nanoparticles. The pellet was resuspended in water for future use.

Synthesis of PEGylated PNCs.—To obtain PNC, the core PBDT-TA nanoparticles were dissolved by DMF. Briefly, 100 μL of the PBDT-TA@PDA nanoparticles was incubated in 1.5 mL of DMF solvent at 60 °C and then shaken at 700 rpm for 12 h to completely disassemble the PBDT-TA complex. For the washing process, the resulting product was spun down by centrifugation (9000g for 10 min), and the supernatant was removed. The pellet was resuspended in water for future use.

For PEGylation, the obtained 1 mL of PNC was first dispersed in 1 mL of bicine buffer (pH 8.5, 10 mM) under generous stirring. Then 100 μL of the SH-mPEG (5 mg mL^{-1} in water) was added and gently stirred for 12 h. The resulting product was purified by centrifugation, and the pellet was resuspended in water for future use.

Synthesis of Dye-Loaded PNCs.—The PEGylated PNCs were first dispersed in 2 mL of bicine buffer (pH 8.5, 10 mM) for 30 min while 15 mM dyes (*e.g.*, MB, AA, NR, or NB) were freshly prepared. We chose MB, AA, NR, and NB dyes, which are approved by US Food & Drug Administration (FDA) and can interact with heparin, changing their absorbance and fluorescence. A 10–25 μL portion of the prepared dyes was added to the solution under generous stirring at 7000 rpm for 12 h. For the washing process, the resulting product was purified by quadruple centrifugation (500 g for 10 min), and the supernatants were used to calculate the loading efficiency. The pellet was resuspended in water for future use.

Stability Test of Dye-Loaded PNCs.—In brief, 200 μL of dye-loaded PNCs was incubated in 1 mL of 10 mM SDS, 10 mM Triton X-100, 10 mM NaCl, 10 mM urea, 10 mM HCl (pH ≈ 2), 10 mM NaOH (pH ≈ 12), DMSO, and DMF. The solution was mixed

using a vortex mixer for 5 s and then incubated for 1 h. Then the samples were spun down by centrifugation (12000g for 10 min), and the supernatant was used to calculate the amount of the disassembled dyes in different conditions.

Computational Section.

Computational Methodology.—The molecular structure of heparin was constructed *via* GLYCAM carbohydrate builder software.[57] Specifically, the four monosaccharide units that were used in this study were YZB, WYS, YuA, and QYS. This pattern was repeated six times to construct the heparin polysaccharide. Dopamine-based tetramers and trimers were used for constructing the PDA molecular structure.[58] Each monosaccharide, PDA tetramer, PDA trimer, and dye was parametrized using Gaussian HF/6-31G* through the WebMO interface.[59,60] All systems employed explicit solvent, which models each water molecule. TIP3P solvent parameters were used exclusively. The generated systems were minimized in seven restrained steps to eliminate bad contacts, heated in one step to 300 K, and equilibrated in seven steps, with each step reducing the imposed restraints on the systems. These preparatory operations and the unrestrained simulations were all completed using AMBER 16 with the ff14SB and GAFF force fields while also utilizing additional parameters provided by GLYCAM.[61–63] All unrestrained simulations were run for 130 ns, with a time step of 2 fs, and at constant temperature and pressure of 300 K and 1 atm, respectively. Visualization and distance analyses were completed using visual molecular dynamic (VMD) and the *cpptraj* module of Amber, respectively.[64,65] Distance analysis was performed to calculate the number of interactions between PNC@NB and heparin. An "interaction" was defined as a measured distance between centers of mass of two moieties that was less than 6.0 Å.

Decomposition Analysis of Gibbs Free Energy.—Free energy analysis was performed on each simulation using the MMPBSA.py module of AMBER. This yielded the contributions of van der Waals, electrostatic, polar, and nonpolar solvation to the energetics of a heparin/PDA interaction. In this context, a destabilizing force is one that inhibits the interaction and is shown as a positive value. A stabilizing force is shown as a negative value and supports the interaction.

Supplementary Material

Refer to Web version on PubMed Central for supplementary material.

ACKNOWLEDGMENTS

REFERENCES

(1). Francis CW Prophylaxis for Thromboembolism in Hospitalized Medical Patients. N. Engl. J. Med 2007, 356 (14), 1438–1444. [PubMed: 17409325]

(2). Weitz JI Low-Molecular-Weight Heparins. N. Engl. J. Med 1997, 337 (10), 688–698. [PubMed: 9278467]

(3). Mackman N Triggers, Targets and Treatments for Thrombosis. Nature 2008, 451 (7181), 914–918. [PubMed: 18288180]

(4). Li W; Johnson DJ; Esmon CT; Huntington JA Structure of the Antithrombin–Thrombin–Heparin Ternary Complex Reveals the Antithrombotic Mechanism of Heparin. Nat. Struct. Mol 2004, 11 (9), 857–862.

(5). Chen IY; Matsa E; Wu JC Induced Pluripotent Stem Cells: At the Heart of Cardiovascular Precision Medicine. Nat. Rev. Cardiol 2016, 13 (6), 333–349. [PubMed: 27009425]

(6). Kaushal R; Bates DW; Landrigan C; McKenna KJ; Clapp MD; Federico F; Goldmann DA Medication Errors and Adverse Drug Events in Pediatric Inpatients. Jama 2001, 285 (16), 2114–2120. [PubMed: 11311101]

(7). Monagle P; Studdert DM; Newall F Infant Deaths Due to Heparin Overdose: Time for a Concerted Action on Prevention. J. Paediatr. Child Health 2012, 48 (5), 380–381. [PubMed: 21679338]

(8). Dix D; Andrew M; Marzinotto V; Charpentier K; Bridge S; Monagle P; de Veber G; Leaker M; Chan AK; Massicotte MP The Use of Low Molecular Weight Heparin in Pediatric Patients: A Prospective Cohort Study. J. Pediatr 2000, 136 (4), 439–445. [PubMed: 10753240]

(9). Arimura J; Poole RL; Jeng M; Rhine W; Sharek P Neonatal Heparin Overdose–A Multidisciplinary Team Approach to Medication Error Prevention. J. Pediatr. Pharmacol. Ther 2008, 13 (2), 96–98. [PubMed: 23055872]

(10). Despotis G; Summerfield A; Joist J; Goodnough L; Santoro S; Spitznagel E; Cox JL; Lappas D Comparison of Activated Coagulation Time and Whole Blood Heparin Measurements with Laboratory Plasma Anti-Xa Heparin Concentration in Patients Having Cardiac Operations. J. Thorac. Cardiovasc. Surg 1994, 108 (6), 1076–1082. [PubMed: 7983877]

(11). Vandiver JW; Vondracek TG Antifactor Xa Levels *versus* Activated Partial Thromboplastin Time for Monitoring Unfractionated Heparin. Pharmacotherapy: J. Human Pharmacology and Drug Therapy 2012, 32 (6), 546–558.

(12). Vera-Aguilera J; Yousef H; Beltran-Melgarejo D; Teng TH; Jan R; Mok M; Vera-Aguilera C; Moreno-Aguilera E Clinical Scenarios for Discordant Anti-Xa. Adv. Hematol 2016, 2016, 1.

(13). Murray DJ; Brosnahan WJ; Pennell B; Kapalanski D; Weiler JM; Olson J Heparin Detection by the Activated Coagulation Time: A Comparison of the Sensitivity of Coagulation Tests and Heparin Assays. J. Cardiothorac. Vasc. Anesth 1997, 11 (1), 24–28. [PubMed: 9058215]

(14). Gertler R; Wiesner G; Tassani-Prell P; Braun S-L; Martin K Are the Point-of-Care Diagnostics Multiplate and ROTEM Valid in the Setting of High Concentrations of Heparin and Its Reversal with Protamine? J, Cardiothorac Vasc. Anesth 2011, 25 (6), 981–986. [PubMed: 21315618]

(15). Ma S.-d.; Chen Y.-l.; Feng J; Liu J.-j.; Zuo X.-w.; Chen X.-g. One-Step Synthesis of Water-Dispersible and Biocompatible Silicon Nanoparticles for Selective Heparin Sensing and Cell Imaging. Anal. Chem 2016, 88 (21), 10474–10481. [PubMed: 27689235]

(16). Li S; Huang P; Wu F Highly Selective and Sensitive Detection of Heparin Based on Competition-Modulated Assembly and Disassembly of Fluorescent Gold Nanoclusters. New J. Chem 2017, 41 (2), 717–723.

(17). Liu Z; Ma Q; Wang X; Lin Z; Zhang H; Liu L; Su X A Novel Fluorescent Nanosensor for Detection of Heparin and Heparinase Based on CuInS2 Quantum Dots. Biosen. Bioelectron 2014, 54, 617–622.

(18). Li Y; Sun H; Shi F; Cai N; Lu L; Su X Multi-Positively Charged Dendrimeric Nanoparticles Induced Fluorescence Quenching of Graphene Quantum Dots for Heparin and Chondroitin Sulfate Detection. Biosen. Bioelectron 2015, 74, 284–290.

(19). Zhu D; Ye J; Hu Y; Wen HM; Kang A; Tang Y-P; Chen J; Shan CX; Cui XB Specific Enrichment Combined with Highly Efficient Solid-Phase Tagging for the Sensitive Detection of Heparin

Based on Boronic Acid-Functionalized Mesoporous Silica Nanospheres. Chem. Commun 2016, 52 (79), 11779–11782.

(20). Xu M; Wang LV Photoacoustic Imaging in Biomedicine. Rev. Sci. Instrum 2006, 77 (4), 041101.

(21). Hu L; Liao H; Feng L; Wang M; Fu W Accelerating the Peroxidase-Like Activity of Gold Nanoclusters at Neutral pH for Colorimetric Detection of Heparin and Heparinase Activity. Anal. Chem 2018, 90 (10), 6247–6252. [PubMed: 29697968]

(22). Qu F; Liu Y; Lao H; Wang Y; You J Colorimetric Detection of Heparin with High Sensitivity Based on the Aggregation of Gold Nanoparticles Induced by Polymer Nanoparticles. New J. Chem 2017, 41 (19), 10592–10597.

(23). Bamrungsap S; Cherngsuwanwong J; Srisurat P; Chonirat J; Sangsing N; Wiriyachaiporn N Visual Colorimetric Sensing System Based on the Self-Assembly of Gold Nanorods and Graphene Oxide for Heparin Detection Using a Polycationic Polymer as a Molecular Probe. Anal. Methods 2019, 11 (10), 1387–1392.

(24). Yoshimi Y; Sato K; Ohshima M; Piletska E Application of the 'Gate Effect' of a Molecularly Imprinted Polymer Grafted on an Electrode for the Real-Time Sensing of Heparin in Blood. Analyst 2013, 138 (17), 5121–5128. [PubMed: 23851360]

(25). Tan L; Yao S; Xie Q Electrochemical Determination of Heparin Using Methylene Blue Probe and Study on Competition of Ba2+ with Methylene Blue for Binding Heparin. Talanta 2007, 71 (2), 827–832. [PubMed: 19071381]

(26). Tian L; Zhao H; Zhao Z; Zhai J; Zhang Z A Facile Voltammetric Method for Detection of Heparin in Plasma Based on the Polyethylenimine Modified Electrode. Anal. Methods 2019, 11 (10), 1324–1330.

(27). Wang J; Chen F; Arconada-Alvarez SJ; Hartanto J; Yap L-P; Park R; Wang F; Vorobyova I; Dagliyan G; Conti PS A Nanoscale Tool for Photoacoustic-Based Measurements of Clotting Time and Therapeutic Drug Monitoring of Heparin. Nano Lett. 2016, 16 (10), 6265–6271. [PubMed: 27668964]

(28). Weber J; Beard PC; Bohndiek SE Contrast Agents for Molecular Photoacoustic Imaging. Nat. methods 2016, 13 (8), 639–650. [PubMed: 27467727]

(29). Chen Y-S; Zhao Y; Yoon SJ; Gambhir SS; Emelianov S Miniature Gold Nanorods for Photoacoustic Molecular Imaging in the Second Near-Infrared Optical Window. Nat. Nanotechnol 2019, 14 (5), 465–472. [PubMed: 30833692]

(30). Chitgupi U; Nyayapathi N; Kim J; Wang D; Sun B; Li C; Carter K; Huang WC; Kim C; Xia J; Lovell JF Surfactant-Stripped Micelles for NIR-II Photoacoustic Imaging Through 12 cm of Breast Tissue and Whole Human Breasts. Adv. Mater 2019, 31 (40), 1902279.

(31). Mantri Y; Jokerst JV Engineering Plasmonic Nanoparticles for Enhanced Photoacoustic Imaging. ACS Nano 2020, 14 (8), 9408–9422. [PubMed: 32806027]

(32). Jeevarathinam AS; Pai N; Huang K; Hariri A; Wang J; Bai Y; Wang L; Hancock T; Keys S; Penny W A Cellulose-Based Photoacoustic Sensor to Measure Heparin Concentration and Activity in Human Blood Samples. Biosens. Bioelectron 2019, 126, 831–837. [PubMed: 30602265]

(33). Feng G; Zhang G-Q; Ding D Design of Superior Phototheranostic Agents Guided by Jablonski Diagrams. Chem. Soc. Rev 2020, 49 (22), 8179–8234. [PubMed: 33196726]

(34). Ou H; Dai S; Liu R; Ding D Manipulating the Intramolecular Motion of AIEgens for Boosted Biomedical Applications. Sci. China Chem 2019, 62, 929–932.

(35). Chen Y-S; Yoon SJ; Frey W; Dockery M; Emelianov S Dynamic Contrast-Enhanced Photoacoustic Imaging Using Photothermal Stimuli-Responsive Composite Nanomodulators. Nat. Commun 2017, 8 (1), 1–10. [PubMed: 28232747]

(36). Lyu Y; Fang Y; Miao Q; Zhen X; Ding D; Pu K Intraparticle Molecular Orbital Engineering of Semiconducting Polymer Nanoparticles as Amplified Theranostics for *in Vivo* Photoacoustic Imaging and Photothermal Therapy. ACS Nano 2016, 10 (4), 4472–4481. [PubMed: 26959505]

(37). Kang J; Kim D; Wang J; Han Y; Zuidema JM; Hariri A; Park JH; Jokerst JV; Sailor MJ Enhanced Performance of a Molecular Photoacoustic Imaging Agent by Encapsulation in Mesoporous Silicon Nanoparticles. Adv. Mater 2018, 30 (27), 1800512.

(38). Qin H; Zhou T; Yang S; Xing D Fluorescence Quenching Nanoprobes Dedicated to *in Vivo* Photoacoustic Imaging and High-Efficient Tumor Therapy in Deep-Seated Tissue. Small 2015, 11 (22), 2675–2686. [PubMed: 25656695]

(39). Brkovic N; Zhang L; Peters JN; Kleine-Doepke S; Parak WJ; Zhu D Quantitative Assessment of Endosomal Escape of Various Endocytosed Polymer-Encapsulated Molecular Cargos upon Photothermal Heating. Small 2020, 16 (46), 2003639.

(40). Siwicka ZE; Son FA; Battistella C; Moore MH; Korpanty J; McCallum NC; Wang Z; Johnson BJ; Farha OK; Gianneschi NC Synthetic Porous Melanin. J. Am. Chem. Soc 2021, 143 (8), 3094–3103. [PubMed: 33600146]

(41). Zhou J; Xu M; Jin Z; Borum RM; Avakyan N; Cheng Y; Yim W; He T; Zhou J; Wu Z; Mantri Y; Jokerst JV Versatile Polymer Nanocapsules *via* Redox Competition. Angew. Chem., Int. Ed 2021, 60, 26357.

(42). Zhou J; Lin Z; Penna M; Pan S; Ju Y; Li S; Han Y; Chen J; Lin G; Richardson JJ Particle Engineering Enabled by Polyphenol-Mediated Supramolecular Networks. Nat. Commun 2020, 11 (1), 1–8. [PubMed: 31911652]

(43). Lee H; Dellatore SM; Miller WM; Messersmith PB Mussel-Inspired Surface Chemistry for Multifunctional Coatings. Science 2007, 318 (5849), 426–430. [PubMed: 17947576]

(44). Yim W; Borum RM; Zhou J; Mantri Y; Wu Z; Zhou J; Jin Z; Creyer M; Jokerst JV Ultrasmall Gold Nanorod-Polydopamine Hybrids for Enhanced Photoacoustic Imaging and Photothermal Therapy in Second Near-Infrared Window. Nanotheranostics 2022, 6 (1), 79–90. [PubMed: 34976582]

(45). Wang J; Jeevarathinam AS; Humphries K; Jhunjhunwala A; Chen F; Hariri A; Miller III BR; Jokerst JV A Mechanistic Investigation of Methylene Blue and Heparin Interactions and Their Photoacoustic Enhancement. Bioconjugate Chem. 2018, 29 (11), 3768–3775.

(46). Cao W; Zhou X; McCallum NC; Hu Z; Ni QZ; Kapoor U; Heil CM; Cay KS; Zand T; Mantanona AJ Unraveling the Structure and Function of Melanin Through Synthesis. J. Am. Chem. Soc 2021, 143 (7), 2622–2637. [PubMed: 33560127]

(47). Yim W; Zhou J; Mantri Y; Creyer MN; Moore CA; Jokerst JV, Gold Nanorod–Melanin Hybrids for Enhanced and Prolonged Photoacoustic Imaging in the Near-Infrared-II Window. ACS Appl. Mater. & Interfaces 2021.1314974 [PubMed: 33761255]

(48). Jokerst JV; Lobovkina T; Zare RN; Gambhir SS Nanoparticle PEGylation for Imaging and Therapy. Nanomed. 2011, 6 (4), 715–728.

(49). Delparastan P; Malollari KG; Lee H; Messersmith PB Direct Evidence for the Polymeric Nature of Polydopamine. Angew. Chem., Int. Ed 2019, 58 (4), 1077–1082.

(50). Wu D; Zhou J; Creyer MN; Yim W; Chen Z; Messersmith PB; Jokerst JV, Phenolic-Enabled Nanotechnology: Versatile Particle Engineering for Biomedicine. Chem. Soc. Rev 2021. 50 4432 [PubMed: 33595004]

(51). Han Y; Lin Z; Zhou J; Yun G; Guo R; Richardson JJ; Caruso F Polyphenol-Mediated Assembly of Proteins for Engineering Functional Materials. Angew. Chem., Int. Ed 2020, 132 (36), 15748–15755.

(52). Jaques L Protamine–Antagonist to Heparin. Can. Med. Assoc. J 1973, 108 (10), 1291. [PubMed: 4122234]

(53). De Waele JJ; Van Cauwenberghe S; Hoste E; Benoit D; Colardyn F The Use of the Activated Clotting Time for Monitoring Heparin Therapy in Critically Ill Patients. Intensive Care Med. 2003, 29 (2), 325–328. [PubMed: 12594595]

(54). Bromfield SM; Barnard A; Posocco P; Fermeglia M; Pricl S; Smith DK Mallard Blue: A High-Affinity Selective Heparin Sensor That Operates in Highly Competitive Media. J. Am. Chem. Soc 2013, 135 (8), 2911–2914. [PubMed: 23406254]

(55). Zhou J; Yim W; Zhou J; Jin Z; Xu M; Mantri Y; He T; Cheng Y; Fu L; Wu Z A Fiber Optic Photoacoustic Sensor for Real-Time Heparin Monitoring. Biosens. Bioelectron 2022, 196, 113692. [PubMed: 34653712]

(56). Xu M; Yim W; Zhou J; Zhou J; Jin Z; Moore C; Borum R; Jorns A; Jokersta JV The Application of Organic Nanomaterials for Bioimaging, Drug Delivery, and Therapy: Spanning Various Domains. IEEE Nanotechnol Mag. 2021, 15, 8.

(57). Kuttel MM; Stçhle J; Widmalm G CarbBuilder: Software for Building Molecular Models of Complex Oligo-and Polysaccharide Structures. J. Comput. Chem 2016, 37 (37), 2098–2105. [PubMed: 27317625]

(58). Chen C-T; Martin-Martinez FJ; Jung GS; Buehler MJ Polydopamine and Eumelanin Molecular Structures Investigated with *ab Initio* Calculations. Chem. Sci 2017, 8 (2), 1631–1641. [PubMed: 28451292]

(59). Trucks G; Frisch M; Schlegel H; Scuseria G; Robb M; Cheeseman J; Scalmani G; Barone V; Petersson G; Nakatsuji H Gaussian 16, Revision B. 01; Gaussian, Inc.: Wallingford, CT, 2016.

(60). Schmidt J; Polik W WebMO Enterprise, version 13.0; WebMO LLC: Holland, MI, 2013.

(61). Case DA; Berryman J; Betz R; Cerutti D; Cheatham Iii T; Darden T; Duke R; Giese T; Gohlke H; Goetz A AMBER 2015; University of California: San Francisco, 2015.

(62). Maier JA; Martinez C; Kasavajhala K; Wickstrom L; Hauser KE; Simmerling C ff14SB: Improving the Accuracy of Protein Side Chain and Backbone Parameters from ff99SB. J. Chem. Theory Comput 2015, 11 (8), 3696–3713. [PubMed: 26574453]

(63). Wang J; Wolf RM; Caldwell JW; Kollman PA; Case DA Development and Testing of a General Amber Force Field. J. Comput. Chem 2004, 25 (9), 1157–1174. [PubMed: 15116359]

(64). Humphrey W; Dalke A; Schulten K VMD: Visual Molecular Dynamics. J. Molecul. Graphics 1996, 14 (1), 33–38.

(65). Roe DR; Cheatham TE III PTRAJ and CPPTRAJ: Software for Processing and Analysis of Molecular Dynamics Trajectory Data. J. Chem. Theory Comput 2013, 9 (7), 3084–3095. [PubMed: 26583988]
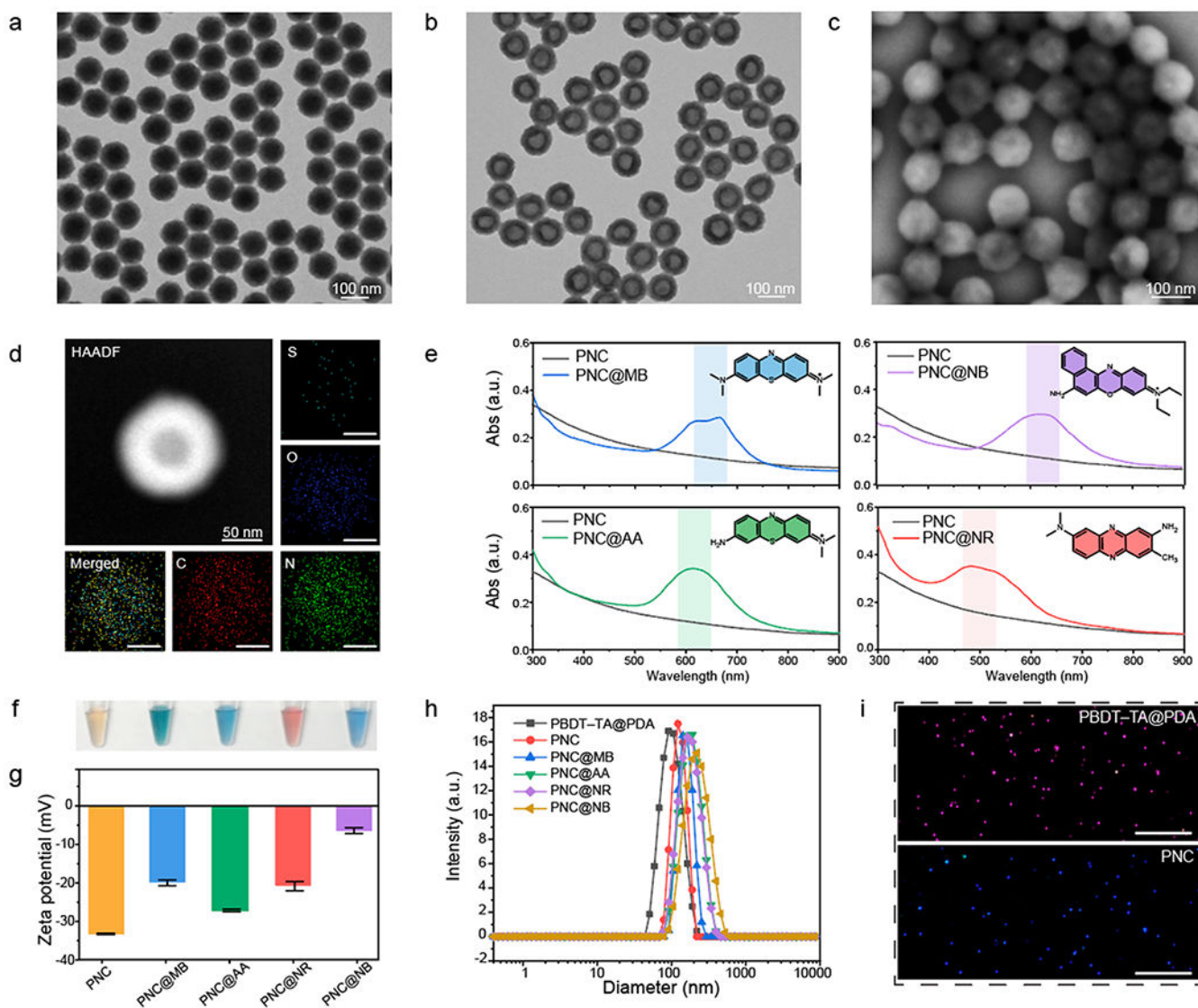
Figure 1.

Dye-loaded PNC. TEM image of (a) PBDT-TA@PDA and (b) PNC. (c) SEM image of PNC. (d) EDX and HAADF-STEM images of PNC. The scale bars represent 50 nm. (e) UV–vis–NIR absorption spectra of PNC@MB, PNC@AA, PNC@NR, and PNC@NB with respect to PNC alone. Black and colored curves represent PNC alone and dye-loaded PNCs. (f) Photograph of PNC (brown), PNC@MB (dark green), PNC@AA (blue), PNC@NR (red), and PNC@NB (blue) in aqueous solution. (g) Zeta potential of PNC, PNC@MB, PNC@ AA, PNC@NR, and PNC@NB. The error bars represent the standard deviation of three separate measurements. (h) DLS data of PBDTTA@ PDA, PNC, PNC@MB, PNC@AA, PNC@NR, and PNC@NB. (i) NTA images of PBDT-TA@PDA and PNC. Pink and blue dots represent monodispersed PBDT-TA@PDA and PNC. The scale bars represent 10 μm.
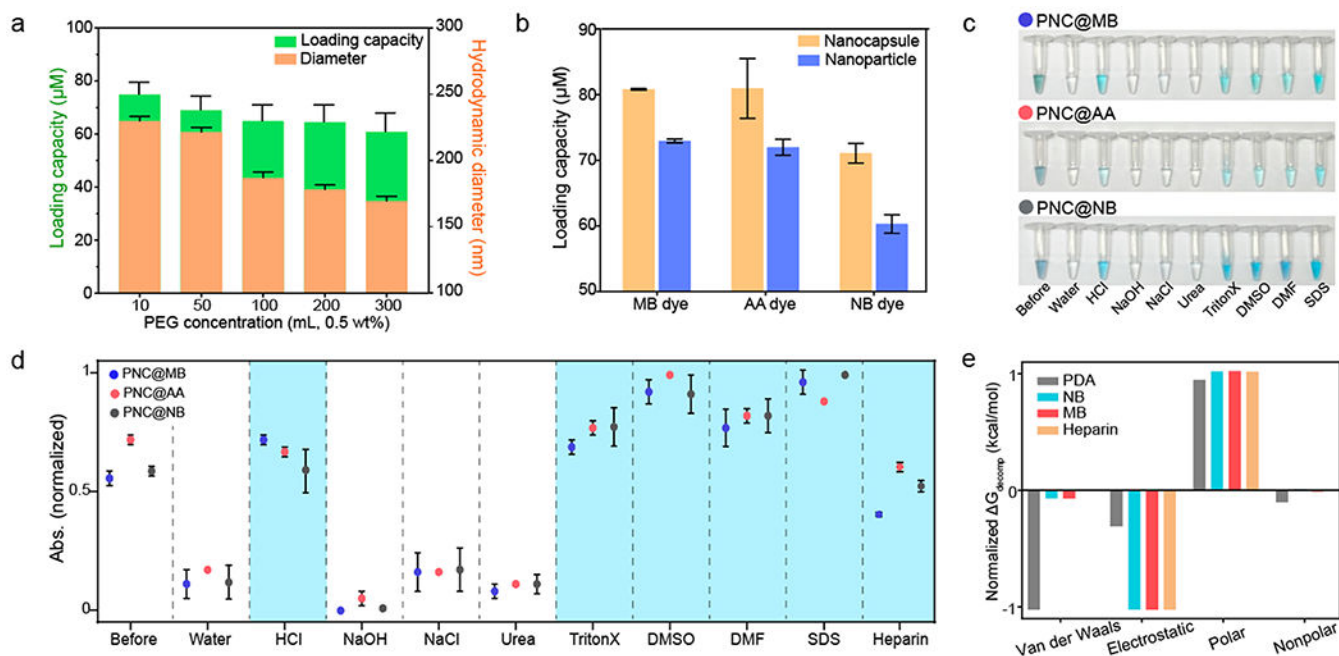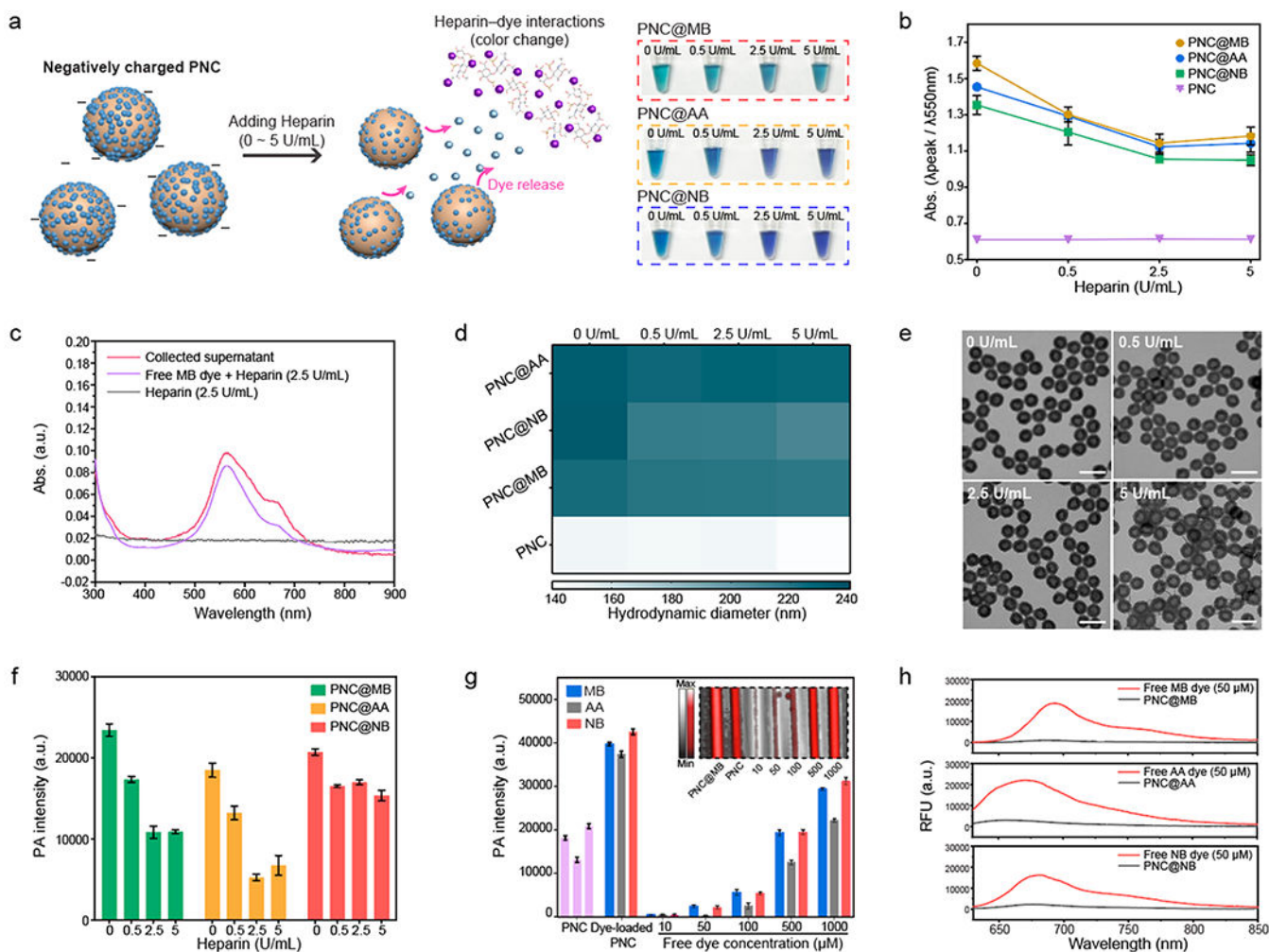
Figure 2.
Dye–PNC assemblies. (a) Loading capacity and hydrodynamic diameter of PNC@MB, where the surface of PNC was modified with different concentrations of HS-mPEG. (b) Loading capacity comparison between PDA nanocapsule and PDA nanoparticle. (c) Photograph of the released dyes in different media (from left to right: before centrifugation, water, HCl, NaOH, NaCl, urea, TritonX-100, DMSO, DMF, and SDS). (d) Quantification of data in panel c: Release of the loaded dye in PNC in different media. Blue area indicates where the loaded dyes were released. (e) Decomposition analysis of the normalized Gibbs free energy of PDA, NB, MB, and heparin using MD simulation. Van der Waals, electrostatic, and polar/nonpolar solvation were investigated for the analysis. The error bars represent the standard deviation of three separate measurements.

Figure 3.

Disassembly of the loaded dyes in negatively charged PNC. (a) Schematic of releasing loaded dyes in negatively charged PNC during heparin interaction. Photograph shows color change of PNC@MB, PNC@AA, and PNC@NB after heparin interaction. (b) Absorbance change of dye-loaded PNC after heparin interaction. The error bars represent the standard deviation of three separate measurements. (c) PNC@MBs were centrifuged down to collect the supernatant after heparin interaction. UV–vis–NIR spectra shows that the absorbance obtained from the collected supernatant was matched with free MB dye–heparin interaction. (d) Hydrodynamic diameter of PNC@MB, PNC@AA, PNC@NB, and PNC after heparin interaction. (e) TEM images of PNC@MB after heparin interaction. The scale bars represent 200 nm. (f) Decrease in PA signal after releasing the loaded dyes in PNC during heparin interaction. The error bars represent the standard deviation of five regions of interest. (g) PA signal comparison between free dyes and dye-loaded PNC that loaded 50 μM dye. Purple bars represent PA signal of PNC alone. The inset image represents the PA image of PNC@MB compared to free MB dye. The error bars represent the standard deviation of five regions of interest. (h) Fluorescence of free MB, AA, and NB dyes compared to MB@PNC,
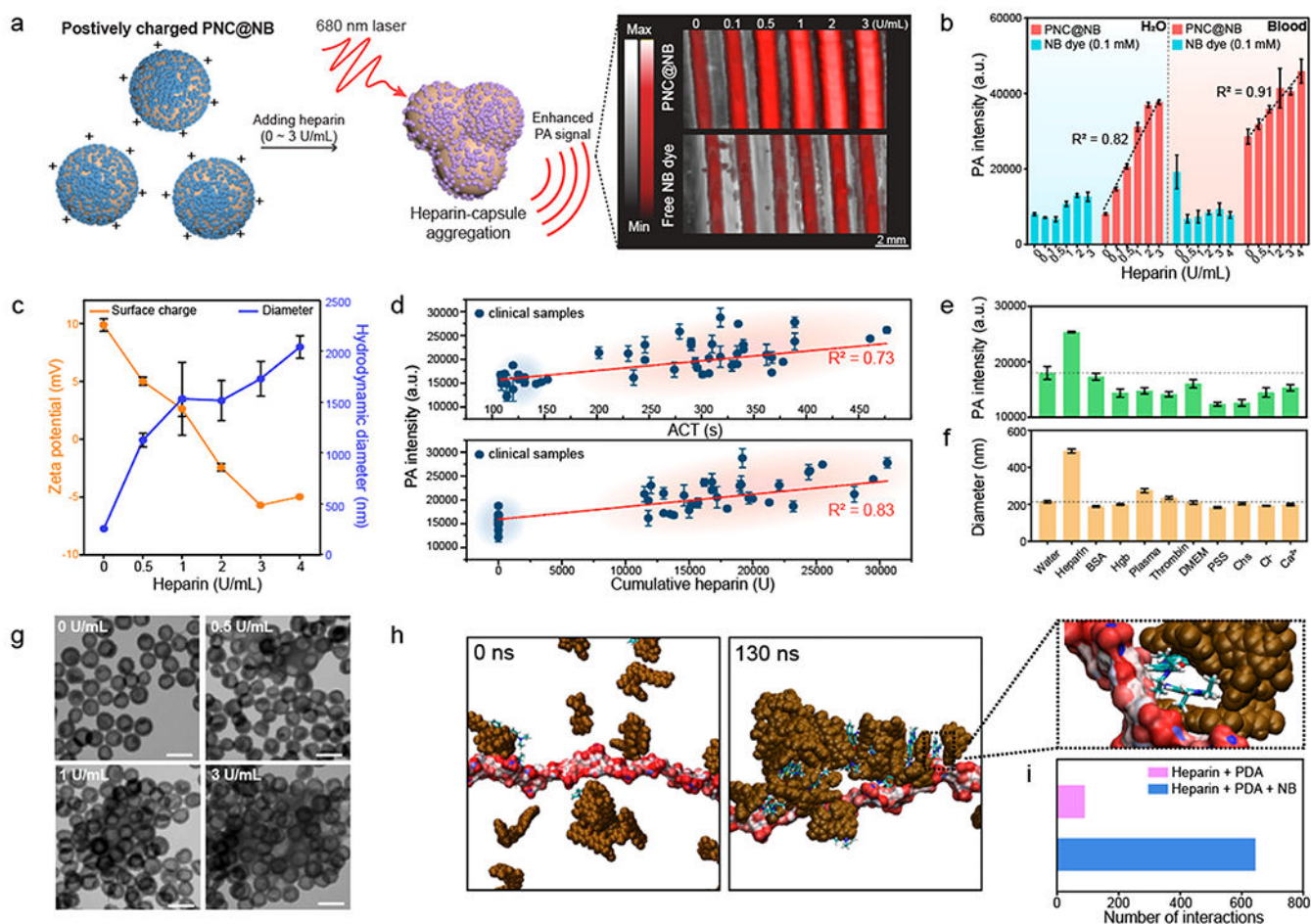
AA@PNC, and NB@PNC that loaded 50 μM dye. The experiments in (f) and (g) were repeated independently three times with similar results.

Figure 4.
Aggregation-induced PA enhancement of positively charged PNC. (a) Schematic of induced PNC@NB–heparin aggregation. Photograph indicates outstanding PA performance of PNC@NB over free NB dye (100 μM) for monitoring heparin. (b) PA signal comparison between PNC@NB and free NB dye at the same dye concentration in either water ($R^2 =$ 0.82) or whole human blood ($R^2 = 0.91$). The error bars represent the standard deviation of five regions of interest. (c) DLS data and the surface charge of PNC@NB after heparin interaction in water. The error bars represent the standard deviation of three separate measurements. (d) PA signal of PNC@NB tested with clinical samples. The PA signal was linearly increased as a function of cumulative heparin ($R^2 = 0.83$) and ACT values ($R^2 = 0.73$). Clinical samples were collected from 17 patients undergoing cardiac procedures. Blue and red regions indicate before (blue) and after (red) heparin infusion. The error bars represent the standard deviation of five regions of interest. (e) PA intensity and (f) corresponding size when PNC@NB interacted with other complex sample matrices. The error bars represent the standard deviation of three separate measurements. (g) TEM images of aggregated PNC@NB during heparin interaction. The scale bars represent 200 nm. (h) Evolution profiles of the size of the complex, comprised of PDA (brown), heparin (red/white), and free NB dye, showing the aggregation in explicit water. Magnified interface section shows that NB dye bridged interaction between PDA and heparin. (i) Number
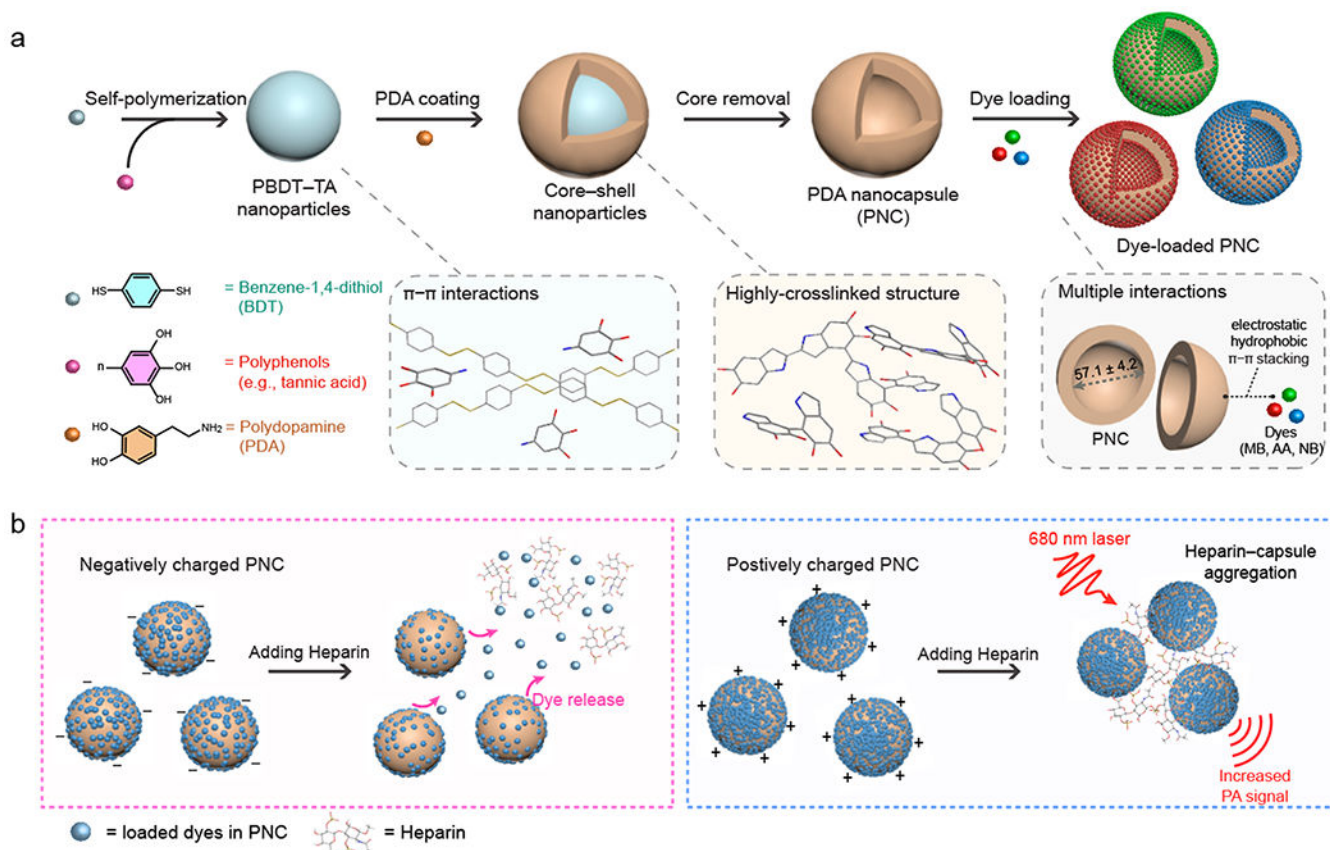
of interactions between heparin and PDA for both PDA+heparin+NB and PDA+heparin systems. The experiments in (b), (d), and (e) were repeated independently three times with similar results.

Scheme 1. Synthetic Pathway and Charge-Dependent Behaviors of Functionalized PNC

(a) Schematic of simple synthesis of dye-loaded PNCs. PNC was synthesized using a supramolecular template (PBDT-TA). By virtue of glue-like nature of PDA, PNC was loaded with small molecular dyes (*e.g.*, NB, AA, and MB) via multiple interactions. (b) During heparin interactions, negatively charged PNCs released the loaded dyes in PNCs, while positively charged PNCs showed particle aggregation that increased PA signal.